Chaos, Solitons and Fractals 173 (2023) 113764

Contents lists available at ScienceDirect

Chaos, Solitons and Fractals

journal homepage: www.elsevier.com/locate/chaos

Self-organization and evolution of structure and function in cultured neuronal networks

L.M. Ballesteros-Esteban [a,b,c,*], I. Leyva [a,b], J.A. Almendral [a,b], I. Sendiña-Nadal [a,b]

[a] Complex Systems Group & GISC, Universidad Rey Juan Carlos, Calle Tulipán s/n, Móstoles, 28933, Madrid, Spain
[b] Center for Biomedical Technology, Universidad Politécnica de Madrid, Campus Montegancedo, Pozuelo de Alarcón, 28223, Madrid, Spain
[c] International Doctoral School, Universidad Rey Juan Carlos, Calle Tulipán s/n, Móstoles, 28933, Madrid, Spain

ARTICLE INFO

Keywords:
Functional network
Neuronal culture

ABSTRACT

Cultured neuronal networks (CNNs) have recently achieved major relevance as an alternative to *in vivo* models. While many works investigate the evolution of functional connectivity alone, experimental evidence of the simultaneous change of the structural neuronal network substrate is scarce. In the present study, we monitored the coevolution of structural and functional connectivities of neuronal cultures grown on top of microelectrode arrays, in a setup that allows the simultaneous recording of electrophysiological signals and microphotography detailed to the single-link level. During the observed 3 weeks lifespan, initially isolated invertebrate neurons form an *ex novo* complex circuitry of neuronal aggregates characterized by a small-world topology, with abundant neuronal loops (high clustering) and short distances. At the same time, the observation of synchronization events among electrodes reaches a maximum, coinciding with the spatial percolation of the neuronal network. At this stage, the correlation between the structural and the corresponding functional network is the largest, with around 15% of the physical links relating electrodes that fire synchronously. As the culture matures, this correlation smoothly declines but becomes more significant. Finally, at the local level, we found that the electrodes supporting the most coherent activity, the functional hubs, are not hubs in the physical circuitry but nodes with an average degree. This study demonstrates that functional networks of self-organized neuronal systems are discreet proxies of the underlying structure. It paves the way for future investigations to elucidate the intricate relationship between structure and function in other scenarios mediated by external stimulation.

1. Introduction

The close interrelation between the structural conformation of a network and its functional dynamics is one of the paradigms of Network Science, and it is paramount to the study of the emergence of coherent collective states [1–4]. An enormous effort has been devoted to understanding this relationship, and the knowledge gathered so far has driven the advances in crucial applications in biological systems, especially in brain dynamics [5,6], the relationship between the central nervous system areas [7] and many others where synchronization is relevant [8,9]. A detailed, quantitative comprehension of this relation and its temporal evolution is of foremost importance because changes in the correlation can help trace pathological deviations as in the case of Alzheimer's or epilepsy [10].

However, the experimental study of this structure–function connection in biological networks is a challenging problem. In the case of brain dynamics [11–13] in most of the studies, the functional data proceeds mainly from resting-state functional magnetic resonance imaging (fMRI), but also electroencephalography (EEG), magnetoencephalography (MEG) or positron emission tomography (PET). The structural network has two primary sources: non-invasive *in vivo* diffusion-weighted MRI, which allows a large-scale indirect inference of the structure, or the invasive tractography or neuronal tracers [14], which permits a more direct mesoscale measurement of the neural paths [15]. The results are very variable across studies, but most of them point to a moderate positive correlation between structural and functional networks in several systems as the human [16], macaque [17], or rat [18] connectomes.

In all the mentioned studies, the spatial resolution of both the functional and the structural measurements corresponds to averages at large to mesoscopic scale. At the microscale, neuroscience has found an excellent tool in cultured neuron networks (CNNs) [13,19,20]. In particular, CNNs grown on devices capable of electrophysiological recording as microelectrode arrays (MEAs) [21–26], high-density

* Corresponding author.
E-mail address: luismiguel.esteban@urjc.es (L.M. Ballesteros-Esteban).

https://doi.org/10.1016/j.chaos.2023.113764
Received 2 June 2023; Accepted 26 June 2023
Available online 10 July 2023

multielectrode arrays (CMOS) [27,28], or in an environment where calcium waves can be measured [29,30], have provided a perfect platform for the study of functional and effective connectivity. These experiments, along with progressively more sophisticated correlation and statistical techniques, have revealed very relevant aspects of the development of the CNNs along their lifespan, as the self-organization of the effective network [26], the role of effective hubs [31], or the emergence of functional small-world properties [32,33] and rich-club [24].

Unfortunately, in all the studies performed on CNNs of mammal neurons, the extreme density and complexity of the network [34,35] make, in practice, impossible to have detailed information of the structural connectivity, and therefore the structure–function correlation at this microscale had to be necessarily indirect. In those cases where the topology of the network was specifically engineered to follow artificial patterns [36–38], the knowledge of the topology is more detailed but still far from the individual node level.

So far, the few studies tackling the node-to-node level in structural connectivity are those based on invertebrate CNNs. Invertebrate models have been used in Neuroscience as a simplified approach to studying complex systems thanks to their basic neuronal features similar to vertebrate ones [39–42]. Their usually large neuronal size (locust neurons are $\sim$ 20–50 mm diameter) facilitates the observation at the node (neuron) and single-link (neurite) levels and thus the monitoring of the circuitry's development [39,43,44]. In Refs. [23,45–47] reported a detailed analysis of the growing level of self-organization in the connectivity of developing CNNs along their lifespan, revealing the emergence of exponential scaling in the degree distribution and small-word properties. Neuronal density also influences the rate of maturation such that denser cultures matures faster and show activity earlier [48,49]. On the contrary, sparser cultures develop a network circuitry that is easier to disentangle. For the present work, we grow medium-density monolayer cultures, $\sim$ 1,200 cells within the $\sim$ 2 mm^2 recording area of microelectrode arrays (MEA) to have simultaneous access to the detailed neuronal connectivity and electrophysiological dynamics. We study the longitudinal evolution of the characteristics of both the anatomical and functional networks derived from microscopy and MEA measures, respectively. Thus, this experimental study is among the first to investigate the direct correlation between the structure and its simultaneous functional counterpart along the culture's development. Our results show that even when the electrical activity and average level of synchronization reduce as the CNNs network matures, the positive structure–function correlation increases as the network ages, becoming more efficient.

2. Results

The present study establishes a longitudinal comparison of the topological properties of the anatomical and functional connectivity of neuronal cultures throughout their different stages of development. It comprises 19 primary neuronal cultures from dissociated frontal ganglia of dessert locusts (*Schistocerca gregaria*) [50] grown on top of MEAs with a regular layout of 120 electrodes and kept for 21 days *in vitro* (DIV). The experimental setup allows us to register the spontaneous activity (without external stimulation) of each culture for 30 min every 1–2 DIV and to take a high spatial resolution image of the culture area ($\sim$ 2 mm^2). A detailed description of the culture protocol and of the image/data acquisition can be found in the Materials and Methods Section.

Results are split into three sections. The first presents topological and morphological network statistics at the level of the physical neuronal circuitry. The second presents statistics on the spike activity at the electrode level and at the level of the functional network. In the third, we statistically compare these two aspects of cultures, their structural circuitry and the underlying dynamical interactions using that circuitry. As a proxy of the former, we will map the actual neuronal network to the connectivity at the electrode level, while for the latter we will use a straight-forward estimating pair-wise correlation of the spike times recorded at the same potential nodes, that is, the 120 electrodes of the MEA. In all cases, statistics have been performed at each age with all those cultures monitored at that specific age.

2.1. Topological and spatial network analysis of the neuronal circuitry

Our neuronal cultures, grown on top of MEA plates, show similar self-organization traits than those observed in Petri dishes [23] or in chip devices [51], that is, randomly scattered neuronal bodies grow new neurites reconnecting among them to finally form a spatial network of interconnected neuronal aggregates similar to the one showed in Fig. 1**a**.

The extraction of the topological network (adjacency matrix) from the optical images is a delicate procedure that requires the isolation of the neuronal bodies and neurites from other elements, like the MEA electrical tracks and the electrodes themselves. We have developed an *ad hoc* image segmentation algorithm that we summarize here, and whose technical details are explained in Materials and Methods. The different phases of the image processing are sketched in Fig. 1. From the acquired image of the MEA culture (panel **a**), the first step is the removal of the electrical wiring of the MEA layout (black grid) from the image while preserving the continuity of the neurites. An example of how this filter works is illustrated in panel **b** for just the area enclosed with a white dashed frame in panel **a**. From this point on, we can apply the algorithm we reported in Refs. [23,45] for images taken from Petri dish cultures to segment the relevant elements from the background (panel **a**): the neurons and neuronal aggregates (red) and the neurites (green). This information is used to construct an adjacency matrix $A = \{a_{ij}\}$ (blue lines) where the centroids of the red areas representing single and neuronal aggregates are the nodes. Two nodes are connected, that is $a_{ij} = 1$, if there is a direct neurite path (green lines) between the red segmented areas (as nodes 12 and 15 in panel **c**) or an indirect path through a neurite bifurcation (as the link between nodes 1 and 3), otherwise $a_{ij} = 0$. Unsupervised algorithm-detected links are represented in blue. The automatic detection is afterwards supervised to ensure the completeness of the reconstruction. For example, the dashed blue links in panel **c** were manually assigned.

To compare the functional connectivity among active electrodes with the underlying neurite circuitry, we mapped this structural connectivity into a second graph $S = \{a^s_{ij}\}$, with dimension 120 × 120, describing the connectivity at the electrode level. In this description, illustrated in Fig. 2**d**, and fully described in Materials and Methods, we consider that two electrodes are connected, $a^s_{ij} = 1$ (magenta links), if near them there is at least one connected neuron or neuronal aggregate. Hence, as a final result, from each image, we obtain two adjacency matrices: the real-space one A with the topological information of the neuronal network, and the electrode-space S as a proxy of the neuronal circuitry resulting from the approximation of the neurons in A to the MEA electrode grid.

Fig. 2 shows the progression of various topological properties of the two network representations, A (panels **a-c**) and S (panels **d-f**), of the physical neural circuitry. The longitudinal analysis of the network topology in both cases reveals similar features to those observed in neuronal cultures on Petri dishes [23,45,47,51]. As shown in panels **a** and **d**, the number of links increases throughout the maturation process of the CNN, while the total number of nodes (with and without connections) remains stable. Consequently, the average degree increases over the course of the DIVs in both networks. To have an insight into how the spatial network grows, we plot in Fig. 2**b** and **e** the number of connected nodes N_c (nodes with at least one link) and the sizes of the first largest S_1 and second largest S_2 connected components (GCC and GCC2 respectively). In both representations, N_c starts to rapidly increase at the same stage of development after DIV 5, when neurons grow their neurites and establish new connections. At the same time, as the GCC and GCC2 progressively recruit nodes, they increase their

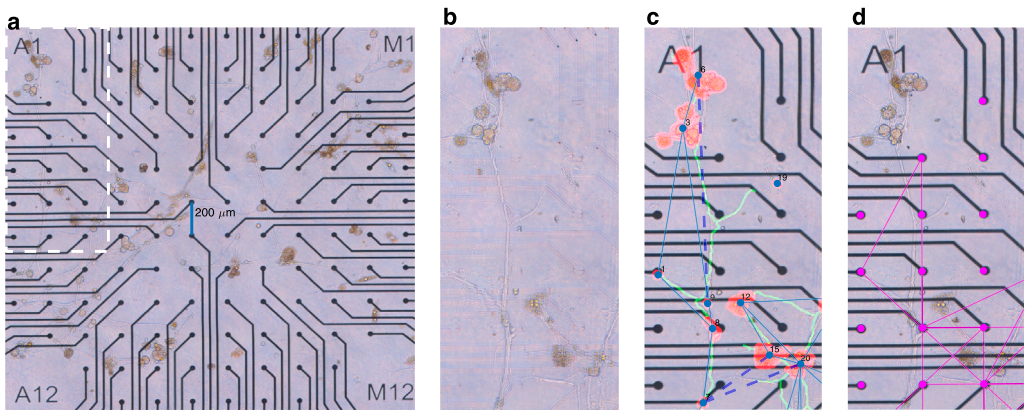

Fig. 1. Image processing steps and extraction of adjacency matrices. (a) Typical snapshot at DIV 9 of a neuronal culture grown on top of a microelectrode array (MEA) with 120 electrodes of 30 μm diameter and 200 μm interspacing. (b) Cut corresponding to the rectangle area framed in (a) after applying the image algorithm that removes the electrode grid, leaving just the neuronal network to which the image segmentation algorithm is applied. (c) Neuronal graph and output of the image segmentation algorithm applied to the region of interest shown in (b). It is superimposed on the electrode layout with the only purpose of showing the accuracy of the graph detection. Single neurons and aggregates are highlighted in red while the processes (neurites) are colored in green. The graph representing the neuronal network is plot on top of the unsupervised (automatic) segmentation result: nodes are the blue circles located at the centroid of each red cluster and links are the blue lines connecting two neuronal aggregates whenever there is a direct process or a path through a bifurcation point. Blue dashed links connecting the pairs $(7,15)$, $(7,20)$, and $(9,6)$ are manually (not automatic) assigned. (d) Electrode graph. Electrodes (magenta circles) are connected (magenta lines) as described in the main text. Red stars represent the centroids of the clusters covering the neuronal aggregate segmented area. The green square represents a neuronal aggregate which has not been assigned to any electrode. See Materials and Methods for a detailed description of how this graph is built. (For interpretation of the references to color in this figure legend, the reader is referred to the web version of this article.)

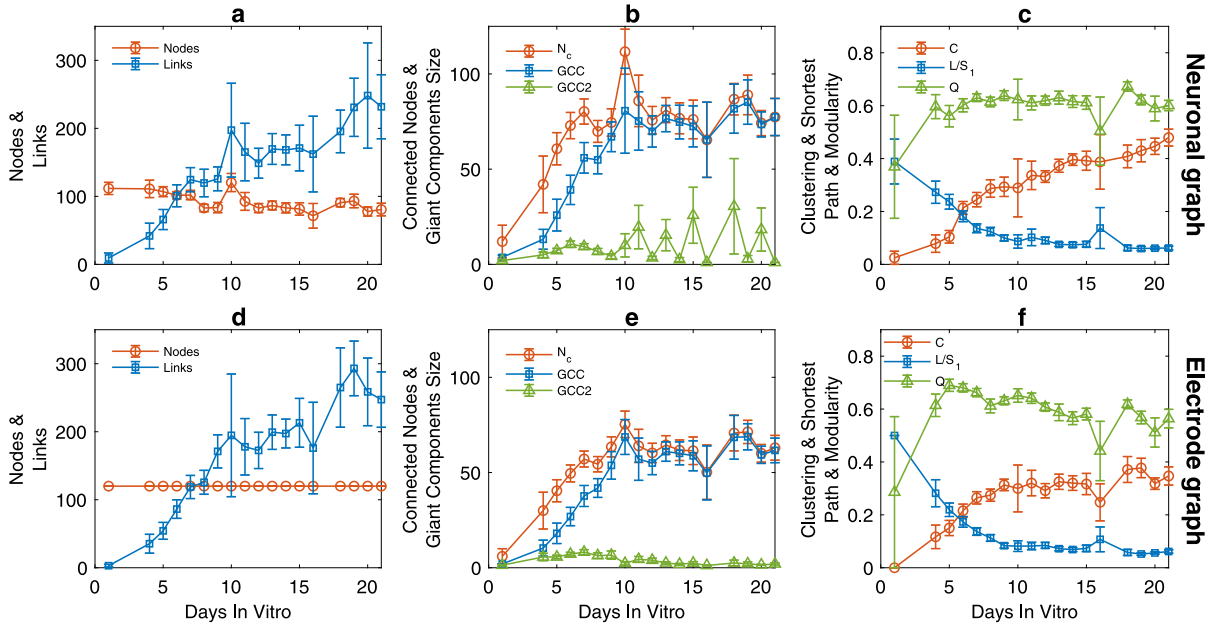

Fig. 2. Basic and complex topological properties of the adjacency matrices at the neuronal and electrode levels as a function of the culture age. (a,d) Number of nodes (red circles) and links (blue squares) for the adjacency matrices describing the neuronal (a) and electrode (d) connectivity. (b,e) Number of connected nodes N_c (red circles, nodes with at least one link), and sizes of the first (GCC, blue squares) and second (GCC2, green triangles) largest components of the neuronal (b) and electrode (e) graphs. (c,f) Clustering coefficient C (red circles), normalized shortest path L/S_1 (blue squares) and modularity Q (green triangles) for both the neuronal (c) and electrode (f) graph representations. Mean values are calculated for 19 cultures at each age from DIV (Days In Vitro) 1 to DIV 21 and error bars represent standard error of the mean.

size up to DIV 10 when the size of the GCC matched that of N_c and the GCC2 practically vanishes, a signature of network percolation in both the real and electrode spaces.

To further assess changes in the network topological state as the cultures mature, we computed the clustering coefficient C, the shortest path L/S_1 (normalized by the size S_1 of the GCC), and the modularity Q of the extracted adjacency matrices A and S (see Refs. [52,53] for definitions). Fig. 2**c** and **f** illustrate the complex evolution of the CNNs architecture for the two types of adjacency matrices, with a significant increase in the clustering coefficient, especially in the first DIVs. They also show a simultaneous decrease in the normalized shortest path L/S_1, whose very low values at the end of the culture's monitorization window indicate that a well-interconnected network has been formed. In addition, since our CNNs are prone to form neuronal aggregates due to tension forces along the neurites, we also calculate the modularity Q as a function of the age. We observe a fast increase in Q during the percolation phase (up to DIV 5–6) and the modularity level is maintained afterwards.

This combined evolution of an increased mean clustering and reduction of the mean shortest path length, supported by a modular structure, characterizes the emergence of a small-world behavior, featuring high efficiency and good segregation-integration capabilities [54]. In addition, since both network representations share the same structural evolution, we feel confident of using the network description at the

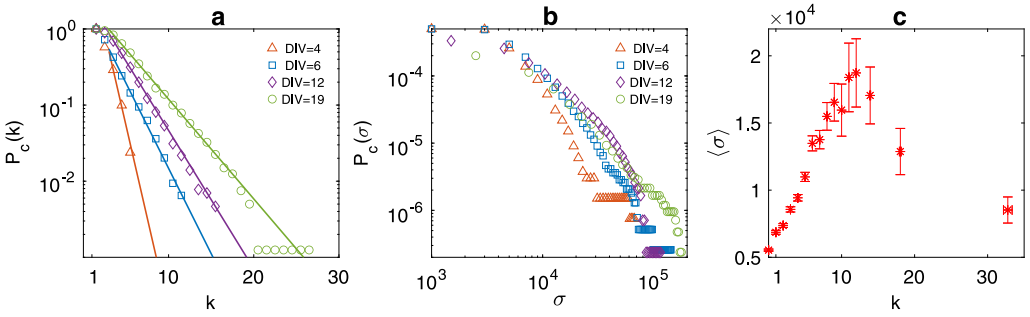

Fig. 3. Node degree and neuronal aggregate area distributions with culture maturation. (a) Semilog cumulative probability distribution $P_c(k)$ of the node degree k in the A adjacency matrix for DIVs 4, 6, 12, and 19 (see legend for symbol encoding). Each straight line is the best exponential fit to $\sim \exp(-k/b)$ with $b \sim \langle k\rangle/4$ and $\langle k\rangle$ the mean degrees at each respective DIV (3.6, 7.8, 9.6, 13.3). (b) Log–log cumulative probability distribution $P_c(\sigma)$ of the neuronal cluster area σ for the same DIVs as in panel a. (c) Relationship between the degree k of a node in the topological network A and the average area $\langle\sigma\rangle$ at any DIV. Areas are in square pixels.

electrode-level as a good coarse-grain approximation to the actual neuronal circuitry.

Beyond the previous network-wide statistics, we assess the relative influence of the nodes and their spatial organization by looking at their node degree k and their spatial size σ (measured as the number of pixels a given neuron or neuronal aggregate occupies in the image). In Fig. 3**a** we plot the cumulative node degree distributions for DIV 4, 6, 12 and 19 on a linear-logarithmic scale. We see a clear increase in the number of high-degree nodes with the age of the culture, leading to a fatter-tailed shape. The data fit an exponential model $\sim \exp(-k/b)$ with large confidence levels ($> 95\%$) (continuous lines in Fig. 3**a**), a signature commonly observed in planar spatial networks whose growth is limited by physical costs [23,47,55,56]. The exponent b scales with the mean degree of all cultures at each age as $\langle k\rangle \sim b/4$, which monotonously increases in the lifespan of the cultures.

Along with the deployment of the connectivity, neurons can migrate due to tension forces, creating aggregates of variable size σ (red areas in Fig. 1**c**). Fig. 3**b** shows the cumulative distributions of the areas $P_c(\sigma)$ on a log–log scale for the same DIVs as in panel **a**. Contrary to the single-scale distributions exhibited by the node degrees with very well-defined characteristic mean degrees, the areas of the neuronal aggregates seem to follow multiscale dynamics with a stretching of the descending tails to a scale-free power-law decay.

One could expect the hubs to be the neuronal aggregates having the largest areas but, counterintuitively, the nodes with medium connectivity are those covering larger areas of the culture. This relationship is shown in Fig. 3**c**, plotting the average value of the area $\langle\sigma\rangle$ as a function of k, at any DIV of the development of the cultures. This relation is due to the aggregation dynamics, driven by the competition between the adhesion force of neuronal bodies to the substrate and the tension along the neurites. Whenever two neuronal clusters aggregate into one, the resulting area increases at the expense of missing the links in common. As a result, the new aggregate has a lower ratio area/connections than the original clusters.

2.2. Spike activity and functional connectivity analysis of the MEA data

Cultures' electrical activity was recorded for 30 min every 1–2 days during their first 3 weeks of development, always before the daily large-scale microscope image was taken. For each detected spike, its peak amplitude, timestamp and electrode number were stored (see Materials and Methods for the definition of spike). Fig. 4 summarizes the global activity dynamics within all recorded preparations during their development in terms of the number of active electrodes (Fig. 4**a**) and the spike rate frequency (Fig. 4**b**). Each point reflects the corresponding activity level for each culture measured at a given DIV. Despite the variability inherent to the use of multiple preparations [48], there are common trends in the 3 weeks of observation. It can be observed that in the initial days of network development (DIVs $0-3$), the cultures are silent with just a few electrodes ($\leq$ 15) detecting extracellular potentials. Concurring with the growth of the GCC (as seen in Fig. 2**a**), the number of active electrodes increases in most of the cultures reaching a maximum of 60 active electrodes around DIV 5 with spiking frequencies up to 0.15 Hz in some of the cultures (panel **b**). Beyond this point, there is an optimization process of the network circuitry with the formation of neuronal aggregates and fusion of parallel neurites as shown in Fig. 2**a**, where the formation of new links is slowed down together with a slight decrease of the number of nodes due to the neuronal aggregation. This stage of development is prolonged up to DIV 15. From this point to the end of the observation period (DIV 21), there is high variability in the cultures' activity. This observation is consistent with previous studies on invertebrate neuronal cultures that reported pronounced changes in the neural firing patterns along this morphological rearrangement during the first two weeks, with a transition from sporadic firing to alternations between active and non-active periods during the recordings [49].

Once we have characterized the topological properties of the structural connectivity, in this section we tackle the analysis of the functional connectivity, which in our case is determined by the pair-wise correlation of the spike time series recorded by the MEA electrodes. There are many techniques to estimate the relationship between signals, being cross-correlation and coherence the most used [57–61]. Here, due to the event nature of the signal, defined by the timestamps whenever a spike is detected, we opted for a simple method based on the relative timings of the events that measure the degree of simultaneity of the appearance of events in different electrodes [57,58] and the main steps involved in the calculation of the weighted correlation matrix $W = \{w_{ij}\}$ are sketched in Materials and Methods. The strength w_{ij} of the event synchronization between electrodes i and j accounts for the number of spike pairs detected by electrodes i and j simultaneously (allowing a time window tolerance of $\Delta = 0.1$ s), such that $0 \leq w_{ij} \leq 1$, being $w_{ij} = 1$ when all the spikes in both signals are fully synchronized. Due to the observed low-frequency activity (Fig. 2**b**), we use long time series (25 min) for calculating the functional correlation matrix W.

To account for the global level of synchronous activity through the culture development, in Fig. 4**c** we plot the average value of the synchronization event matrix $\langle W\rangle$ for every culture as a function of DIV. A systematic increase of the network-synchronization level starts at DIV 5, a couple of days after cultures become active, and lasts up to DIV 12 where it drops despite spike activity is still relatively high (panels **a** and **b**). Low levels of synchronization are often related to excitatory–inhibitory imbalances [62,63]. On the other hand, structurally, this lack of synchronization patterns coincides indeed with an appreciable rise in the formation of new physical links around DIV 15 (see Fig. 2**a**) after the rearrangement period of two weeks from a state of isolated neurons into a network of neuronal aggregates. It is not clear whether a change in the activity patterns could drive a transformation of the physical circuitry or the other way around.

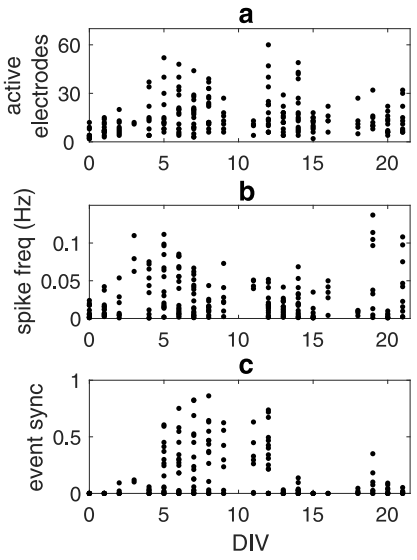

Fig. 4. Spike activity and network-synchronization with culture development. Scatter plots of (a) the number of active electrodes and (b) spike frequency (total number of spikes per active electrode and recording time ratio) for each culture as a function of the culture age. (c) Scatter plot of the mean values of the weighted event synchronization matrices W for each of the 19 cultures monitored over 3 weeks.

2.3. Correlation between structural and functional connectivities

Results presented thus far have focused on two separate aspects of the CNNs evolution: on one hand, identifying changes in the network infrastructure through various topological measures, and on the other hand, considering the evolution of the electrophysiological activity and global synchronization of the cultures. Here, the results focus on how both features compare along the maturation process. Structure–function correlation in neural systems is a controversial question that has attracted attention for a long time [64–67]. However, most studies have only partial evidence of structural connectivity and/or an indirect and coarse measure of neural activity. To our knowledge, our setup is the first experimental case where detailed and longitudinal structural measures at the individual neuron level are paired with direct electrophysiological measures.

To simplify this comparison, we define the functional network $F = \{a^{\mathrm{f}}_{ij}\}$ as the binarized version of the event-synchronization matrix, such that there is functional link $a^{\mathrm{f}}_{ij} = 1$ between nodes i and j if $w_{ij} > 0$, and $a^{\mathrm{f}}_{ij} = 0$ otherwise. Fig. 5**a–b** shows the structural $S = \{a^{\mathrm{s}}_{ij}\}$ (panel **a**) and the corresponding binarized event-synchronization functional $F = \{a^{\mathrm{f}}_{ij}\}$ matrices (panel **b**) at the electrode level for a representative culture at DIV 11. Panels **c** and **d** depict the corresponding spatial arrangements in the MEA of the same matrices, revealing the existence of links between distant electrodes in both the structural and functional descriptions, as well as a high level of modularity as corresponds at this stage of the culture maturation (see Fig. 2**f**). To quantify the comparison, we computed the ratio R of structural links that are actually used to generate synchronized events between different electrodes defined as:

$$R = \frac{1}{L_{\mathrm{s}}} \sum_{i}^{N} \sum_{j>i}^{N} a^{\mathrm{s}}_{ij}\, a^{\mathrm{f}}_{ij} \tag{1}$$

where $N = 120$, and $L_{\mathrm{s}} = \sum_i \sum_{j>i} a^{\mathrm{s}}_{ij}$ is the total number of structural links. For those pair of electrodes (i, j) such that $a^{\mathrm{f}}_{ij}\, a^{\mathrm{s}}_{ij} = 1$, it means that an existing structural link supports some degree of coordination, whereas a null contribution means that either the physical link does not exist ($a^{\mathrm{s}}_{ij} = 0$), or that it exists but has not resulted in any synchronous event ($a^{\mathrm{f}}_{ij} = 0$).

This structural/functional correlation R is plotted in Fig. 5**e** as a function of DIV, where each black dot corresponds to a daily register of each culture, and the red stars to the average values for each DIV. We begin the comparison at DIV 5 since before that stage the structural network is mostly unconnected and, therefore, we find a too-low event synchronization register. As it has often been reported, the global correlation is never too high [66,67]. In our neuronal cultures, we find a maximum ratio of about 15% of structural links registering synchronous activity. Longitudinally, we can observe a clear dependence on the DIV: the correlation peaks around DIV 5–6, which corresponds to the stage of network percolation and maximal synchronization, as shown in Fig. 2**e** and Fig. 4**c** respectively. After that stage, the network is still active, but probably, the formation of neuronal aggregates worsens the synchrony and delayed temporal correlations should be considered instead. To check the significance of this correlation, we compared the obtained values of R against those expected in equivalent random null networks for the functional network F with the same number of nodes and links. In Fig. 5**f** we plot the ratio R/R_{null} as a function of DIV, where R_{null} is the average value of R over 100 instances of randomized version F for each experiment. We observe that most of the cultures are well above the threshold $R/R_{\mathrm{null}} = 1$ (dashed black line) and, thus, the significance of the functional connectivity as a (discreet) proxy of the underlying structural network, even for low values of R, is consistent. We also notice that even when the average R slightly decreases with DIV, its significance grows along the maturation process.

From Fig. 5**a** similarity can be glimpsed between connected modules of electrodes in S and F. To have a deeper insight into this relationship at the local electrode level over the culture lifespan, in Fig. 6, we compare, for three representative days, the electrode activity (registered spikes) to its structural $\hat{k}_{\mathrm{s}}$ and functional $\hat{k}_{\mathrm{f}}$ normalized degrees in the respective S and F adjacency matrices. All the measures have been normalized to compare different stages of CNN's maturation. As expected, there is a clear positive correlation between the firing activity of an electrode and its functional degree k_f (bottom row in Fig. 6), which is strengthened as the culture matures. However, we find that, in general, the most active electrodes are those with intermediate values of physical links, as shown in the upper panels of Fig. 6. This correlation is maintained even in the later stages of the evolution (DIV 18, last column) with a very reduced activity and mostly sustained exclusively by those medium-degree electrodes. Additional mesoscale measures, such as betweenness or eigenvector centrality, could give further information about the central role of those nodes.

3. Discussion and conclusions

The present study compares the CNNs evolution derived from electrophysiological recordings and images capturing the neuronal physical circuitry. From the very first days up to their mature state, neuronal cultures develop a self-organized network structure and a spontaneous firing activity that mutually interact. Although network state evolution can differ depending on multiple factors like the type of neuronal culture or neuronal density, the formation of a giant connected component is crucial for the emergence of higher firing rates and synchronous activity. This network percolation takes place around the second week in rodent cultures [26], whereas in our locust cultures occurs at the end of the first week and coincides with the maximum activity. Synchronization events among electrode recordings mainly occur at this stage, in agreement with data reported in the literature [26,32,68].

After the percolation point, where the networks show a random architecture, our CNNs self-organize into a stable small-world structure with similar topological properties to those previously observed in the literature [23,32]. This mature configuration implies a change in activity patterns. As the culture matures further, electrodes detect less activity, which might be due to the existence of silent neurons, cellular death, or the formation of large neuronal aggregates.

We face the construction of our functional networks using the extracellular signals recorded on each electrode which may be from

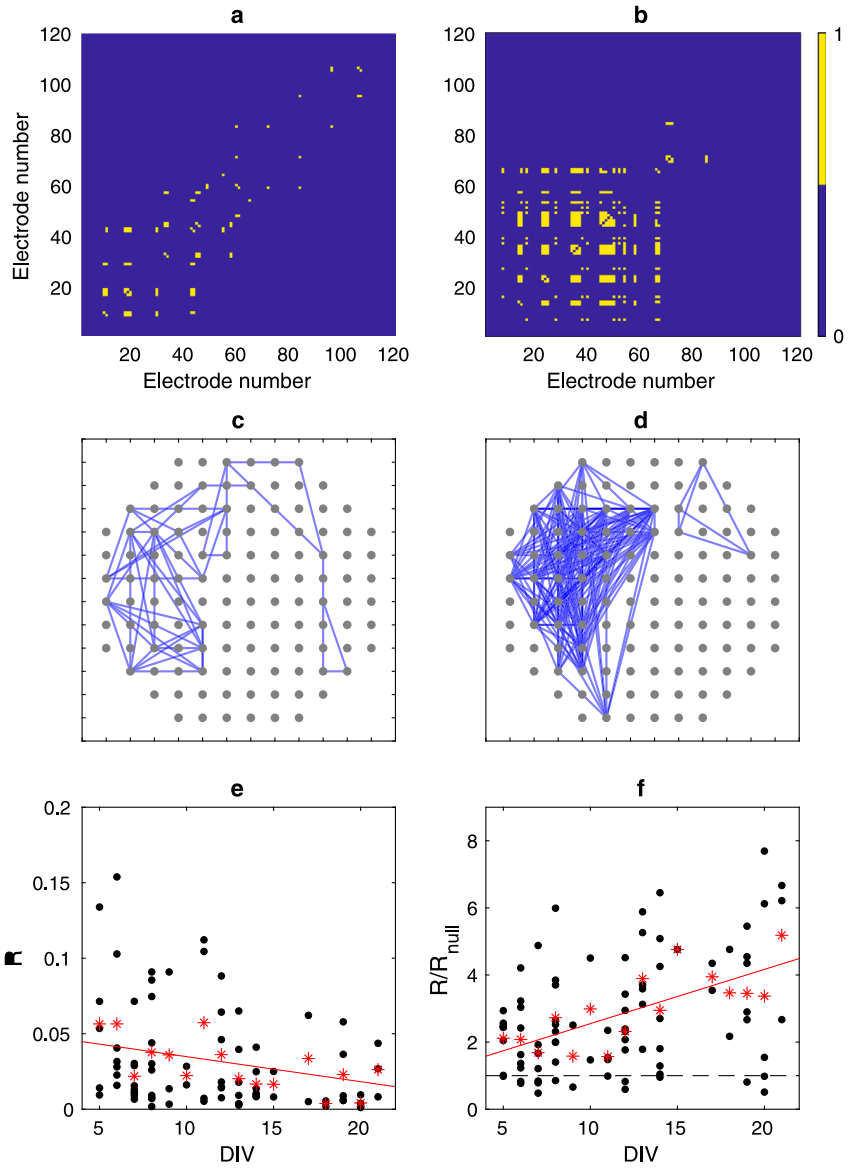

Fig. 5. Structure–function relationship. (a–d) Representative illustration of the comparison between (a) the structural S and (b) functional F connectivity matrices at the electrode level and their corresponding (c) and (d) spatial arrangements on the MEA layouts of one culture at DIV 11. (e) Structure–function correlation R and (f) its null-normalized correlation R/R_{null} (see the main text for definitions). Each black dot corresponds to a daily measure of each culture and stars are mean values for each DIV. Red straight lines are linear fits. In panel (f) the black dashed line marks the significance threshold of 1.

multi-neuron activity, aggregated or not, bringing up another possible source of discrepancies with other studies [49]. In the presented results, we have implemented our synchronization measure as a simple scheme of event synchronization within a time tolerance, but other more sophisticated measures, such as symmetric mutual information or adaptive event synchronization, provide similar results.

To the authors' knowledge, this is the first study of the coevolution of structure and dynamics in self-organized cultured neuronal networks to the level of single links. We find evidence that the link-by-link correlation between structure and persistent functional networks (estimated over 25 min) shows the use of around 10% of the physical links and becomes more significant with the age of the culture. We inspected the degree of connectivity of the active nodes in both the structural and functional layers along the culture lifespan, concluding that the functional hubs that mainly sustain the coherent activity are not the structural hubs but nodes with intermediate degrees. This result suggests that even in very simple cases such as the CNNs cultures, one should be cautious when extrapolating the functional features to the underlying unknown topology [60,69].

Future work will focus on assessing the influence of stimulation on shaping the network structure through culture development and investigating the role of anatomical hubs on self-organized structures in controlling the functional interactions when they are being externally forced.

4. Materials and methods

4.1. Culture protocol

In this work, we used primary neuron cultures from the frontal ganglion of desert locust invertebrates. This nervous structure is involved in the motor functioning of foregut muscles, feeding and molting behavior, and has a well-known cytoarchitecture with approximately 100 neurons [70]. We kept the adult locusts under a 12 – 12 light-dark cycle and fed them daily with organic spinach. After having them anesthetized with CO_2, we dissect the frontal ganglion [70] of 15 locusts to obtain an intermediate neuron density (1200 neurons per culture), following the protocol described in Ref. [40].

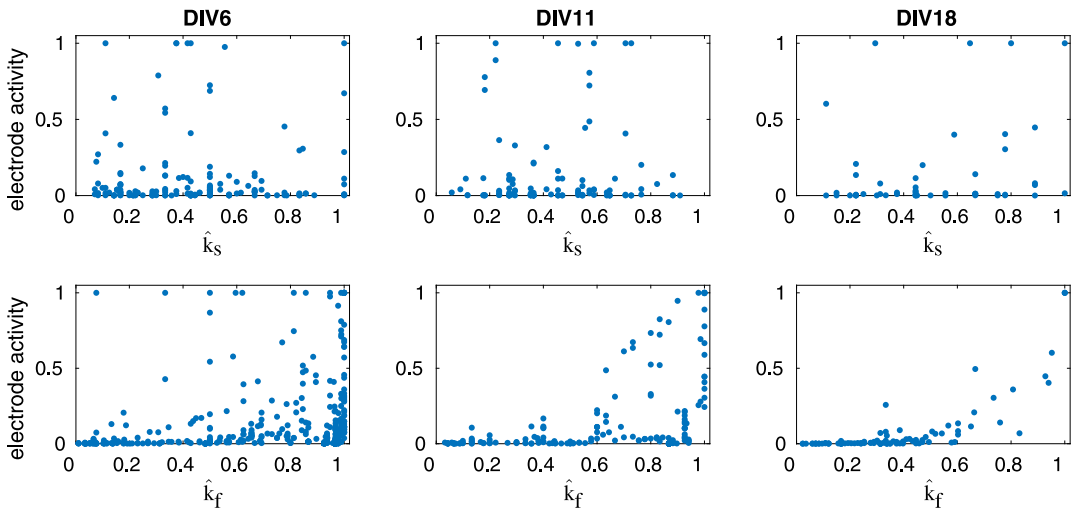

Fig. 6. Local structure–function relationship. Correlation between the (normalized) spike rate of each electrode and its corresponding normalized structural $\hat{k}_s$ (upper row) and functional $\hat{k}_f$ (bottom row) degrees for three representative DIV along the cultures maturation process. Each panel corresponds to a given DIV and contains the individual electrodes' data of all cultures measured that day. All quantities are normalized by the corresponding maximum value observed in each culture that DIV.

The extracted ganglia are immersed in an enzymatic treatment with 500 μl collagenase/dispase (Merck, COLLDISP-RO) mixture (2mg/ml) for 1h, after which the enzyme is replaced with Leibowitz 15 medium (Merck, L1518). Then the ganglia are mechanically dissociated by passing them through a 200 µl pipette tip to separate the neurons and remove any remaining connection. The resulting suspension of neuronal soma is placed on a Concanavalin-A (Merck, C0412, 0.2 mg/ml) and Poly-D-Lysine (Merck, mol wt 70 K–150 K, 0.016 mg/ml) pre-coated area of 2 mm^2 on the glass surface of a microelectrode array with 120 electrodes (Multichannel Systems, 120MEA200/30iR-Ti-pr). After 2 h at dark, seeded neurons adhered to the surface. At that moment, we added 2 ml of Leibowitz 15 enriched with 5% hemolymph extracted from adult specimens and filtered twice (using 0.45 µm and 0.20 µm filters) to enhance neurite growth and covered the culture with a gas-permeable transparent film. The cultures were kept in darkness at 30 °C under controlled humidity (70%), and the medium was not changed at any moment.

Cultures were kept *in vitro* for a maximum of 21 days after platting (DIV 21). The data analyzed in this work are from 19 different cultures and only those lasting at least 12 days were considered in this study.

4.2. Data acquisition

CNNs were measured daily by acquiring an optical microscopy image and recording the electrophysiological signal during their lifespan.

Large-scale images were taken with a phase contrast inverted microscope (Eclipse Ti-S, Nikon) equipped with a 10x air objective (Achromat, ADL, NA 0.25), an automated motorized XYZ stage controller (H117 ProScan, Prior Scientific) and a charge-coupled device camera (DS-Fi1, Nikon) controlled by the NIS-Elements software (Nikon Instruments Software, Nikon). The high-resolution mosaic images are stored in .jp2 files.

Before each image acquisition, the MEA (12 × 12 layout of 120 electrodes of 30 mm diameter and 200 mm spacing) electrophysiological signals were recorded for 30 min (except for DIV 0, which was only 20 min) at dark and at constant temperature of 30 °C and humidity of 70% using a climate chamber (Multichannel Systems, MEA2100-CO2-C) and a temperature controller (MSC, MEA2100-TC02). No chemical or electrical stimulation was applied. Data acquisition was recorded, preprocessed, and stored using the Multi Channel Experimenter V2.20.0 software. Raw signals are preprocessed using a 200–1000 Hz Butterworth Order 2 filter to reduce the noise. Then, the filtered signal is stored as H5 files using Micro Channel Data Manager V 1.14.6.

For the data analysis, we discarded the first 5 min of the signal to eliminate noise and artefacts induced by the culture transfer to the MEA headstage [68,71]. Spikes timestamps were detected offline at each electrode using an adaptive threshold of $\pm 6\sigma$ calculated in a moving window of 1 s as done in Ref. [49] and an electrode was considered active if more than 5 spikes were detected in the 25-min recording segment used. The *ad hoc* code was written for Matlab R2020b. In this study, we considered only negative amplitude spikes.

Data statistics for each day were obtained from at least 3 cultures. Potential outliers were filtered using the standard criterion of median absolute deviation from the median.

4.3. Correlation matrix W

To quantify the pair-wise event synchronization between electrode signals, we calculate the coherence between electrodes i and j as the correlation between the time series of spikes. Once the timestamps are determined, the total time $T = 1500$ s is divided into Γ time bins of size Δ s. Each spiking sequence is converted into a binary series by assigning the value $B_i(\tau) = 1$ if node i spiked within the τ-th bin, and 0 otherwise. The correlation matrix $W = \{w_{ij}\}$ accounts for the event coherence between electrodes i and j, allowing for a tolerance of $\pm\Delta$ as [58]:

$$w_{ij} = \frac{\sum_{\tau=1}^{\Gamma} B_i(\tau)B_j(\tau) + \sum_{\tau=1}^{\Gamma-1} B_i(\tau)B_j(\tau+1) + \sum_{\tau=2}^{\Gamma} B_i(\tau)B_j(\tau-1)}{3\max(\sum_{\tau=1}^{\Gamma} B_i(\tau), \sum_{\tau=1}^{\Gamma} B_j(\tau))} \quad (2)$$

The bin size $\Delta = 0.1$ s is chosen according to the spiking statistics of the experiment to avoid two spikes in the same time bin. As previously stated in the main text, we have tested other common measures to quantify the pair-wise coherence, such as symmetric mutual information [72] or adaptive event synchronization [57], but those measures provide similar results. Therefore, we have opted for presenting the simplest of them.

4.4. Image segmentation

We used a homemade image segmentation algorithm previously developed in Ref. [45] to extract the neuronal network. Since the algorithm was developed for CNNs grown in Petri dishes, for the present study we had to introduce a new filter to remove the artefacts caused by the MEA grid. It is not possible to reconstruct the neuronal network without first eliminating the electrical tracks, as any detection algorithm tends to mislead the tracks with the neurite processes.

The idea behind the filter to remove the MEA grid layout is to fill the black tracks with adjacent pixels. More in detail, the original image Fig. 1**a** is first read by columns trying to locate the vertical paths, which will become coded as one-dimensional blocks of typically 50 black pixels (in this step, horizontal paths are avoided). The next step is to replace the half-right of the block with the information adjacent to the half-right and the same for the left half of the block. Then, the same process is repeated row by row to detect the horizontal tracks and replace each block with the information above and below the blocks. These two scans are sufficient to remove all the tracks, even the diagonal ones as seen in the image cut shown in Fig. 1**b**. Using this procedure, we can recover, at least partially, the continuity of those elements of interest (neurons and neurites) located on top of the layout grid.

Although the tracks and some regions with ripple artefacts are still visible, they do not interfere significantly with the next step: the automatic segmentation process fully described in Ref. [46]. The segmentation algorithm starts from the red layer of the filtered full RGB image, which is segmented and thresholded to separate the background from the foreground containing the neurons and neurites. Then neurons, aggregates and neurites are identified separately [red areas and green paths respectively in Fig. 1**c**]. As mentioned above, the image is segmented with the filtered electrodes. The result is superimposed on the culture image with the grid layout to illustrate how well the algorithm correctly detects neurites and neurons.

4.5. Projection of the neuronal network (A) into the electrode network (S)

To compare the functional connectivity among active electrodes with the underlying neurite circuitry $A = \{a_{ij}\}$, we have to project the latter into a graph of the same dimension as the electrode array, that is, $S = \{a^s_{ij}\}$ has dimension 120×120. We consider that two electrodes i, j are connected $a^s_{ij} = 1$ if close to them there are neurons or neuronal aggregates mutually connected. If a neuronal aggregate covers a large extension, it can be close to two or more electrodes, as node 15 in Fig. 1**c**. In those cases, we decide that the two (or more electrodes) are connected, even when there is only one neuronal aggregate. Therefore, in this step, we need the connectivity matrix S and the size and pixels conforming to the neuronal aggregates (red areas). Using this information, we can identify one or more centroids in each neuronal aggregate using a k-means algorithm. These centroids are marked with red stars in Fig. 1**d**. The number of centroids depends on the size of the segmented area. Individual neurons, typically having 5000–10 000 pixels, will have one centroid and aggregates with 10 000–20 000 pixels, two centroids, and so on. Once the new set of centroids of each neuronal aggregate is placed, we define the electrode connectivity using their distance to these centroids such that two electrodes are connected if there are centroids closer than the 60% the electrode separation (200 μm) that are connected themselves. With this definition, if the centroids closest to the electrodes belong to the same neuronal aggregate, the two electrodes are consequently connected. This criterion justifies the observation given above. For example, a large aggregate with two centroids can induce the connection between two electrodes if each centroid is near each electrode. Moreover, a given neuronal aggregate may be far from any electrode, as is the case of node 6 in Fig. 1**c**, which has four centroids and none of them is close to any electrode. That node is shown as a green square because it does not contribute to the connectivity between electrodes despite the large size of the associated neuronal aggregate.

CRediT authorship contribution statement

L.M. Ballesteros-Esteban: Conducted the experiments, Analyzed the results, Wrote and reviewed the manuscript. **I. Leyva:** Analyzed the results, Wrote and reviewed the manuscript. **J.A. Almendral:** Analyzed the results, Wrote and reviewed the manuscript. **I. Sendiña-Nadal:** Analyzed the results, Wrote and reviewed the manuscript.

Declaration of competing interest

The authors declare the following financial interests/personal relationships which may be considered as potential competing interests: L. Ballesteros-Esteban reports financial support was provided by Rey Juan Carlos University.

Data availability

Data will be made available on request.

Acknowledgments

This research was supported by the Spanish Ministerio de Ciencia e Innovación (Project PID2020-113737GB-I00) and by the Rey Juan Carlos University (PREDOC20-036).

References

[1] Pecora LM. Synchronization conditions and desynchronizing patterns in coupled limit-cycle and chaotic systems. Phys Rev E 1998;58:347–60. http://dx.doi.org/10.1103/PhysRevE.58.347.
[2] Barahona M, Pecora LM. Synchronization in small-world systems. Phys Rev Lett 2002;89:054101. http://dx.doi.org/10.1103/PhysRevLett.89.054101.
[3] Boccaletti S, Latora V, Moreno Y, Chavez M, Hwang D-U. Complex networks: Structure and dynamics. Phys Rep 2006;424(4–5):175–308.
[4] Arenas A, Díaz-Guilera A, Kurths J, Moreno Y, Zhou C. Synchronization in complex networks. Phys Rep 2008;469:93–153. http://dx.doi.org/10.1016/j.physrep.2008.09.002.
[5] Bullmore E, Sporns O. Complex brain networks: graph theoretical analysis of structural and functional systems. Nat Rev Neurosci 2009;10:186–98. http://dx.doi.org/10.1038/nrn2575.
[6] Gosak M, Milojević M, Duh M, Skok K, Perc M. Networks behind the morphology and structural design of living systems. Phys Life Rev 2022;41:1–21.
[7] Schnitzler A, Gross J. Normal and pathological oscillatory communication in the brain. Nat Rev Neurosci 2005;6(4):285–96.
[8] Pluchino A, Latora V, Rapisarda A. Changing opinions in a changing world: a new perspective in sociophysics. Internat J Modern Phys C 2005;16:515–31. http://dx.doi.org/10.1142/S0129183105007261.
[9] Fujiwara N, Kurths J, Díaz-Guilera A. Synchronization in networks of mobile oscillators. Phys Rev E 2011;83:025101. http://dx.doi.org/10.1103/PhysRevE.83.025101.
[10] Sun Y, Yin Q, Fang R, Yan X, Wang Y, Bezerianos A, et al. Disrupted functional brain connectivity and its association to structural connectivity in amnestic mild cognitive impairment and Alzheimer's disease. PLoS One 2014;9(5):e96505.
[11] Batista-García-Ramó K, Fernández-Verdecia CI. What we know about the brain structure–function relationship. Behav Sci 2018;8(4):39.
[12] Wirsich J, Perry A, Ridley B, Proix T, Golos M, Bénar C, et al. Whole-brain analytic measures of network communication reveal increased structure-function correlation in right temporal lobe epilepsy. NeuroImage: Clin 2016;11:707–18.
[13] Chiappalone M, Pasquale V, Frega M. In vitro neuronal networks: from culturing methods to neuro-technological applications. Vol. 22. Springer; 2019.
[14] Gong G, He Y, Concha L, Lebel C, Gross DW, Evans AC, et al. Mapping anatomical connectivity patterns of human cerebral cortex using in vivo diffusion tensor imaging tractography. Cerebral Cortex 2009;19:524–36. http://dx.doi.org/10.1093/cercor/bhn102.
[15] Straathof M, Sinke MR, Dijkhuizen RM, Otte WM. A systematic review on the quantitative relationship between structural and functional network connectivity strength in mammalian brains. J Cereb Blood Flow Metabol 2019;39(2):189–209.
[16] Fukushima M, Betzel RF, He Y, van den Heuvel MP, Zuo X-N, Sporns O. Structure–function relationships during segregated and integrated network states of human brain functional connectivity. Brain Struct Funct 2018;223(3):1091–106.
[17] Miranda-Dominguez O, Mills BD, Grayson D, Woodall A, Grant KA, Kroenke CD, et al. Bridging the gap between the human and macaque connectome: a quantitative comparison of global interspecies structure-function relationships and network topology. J Neurosci 2014;34(16):5552–63.
[18] Diaz-Parra A, Osborn Z, Canals S, Moratal D, Sporns O. Structural and functional, empirical and modeled connectivity in the cerebral cortex of the rat. Neuroimage 2017;159:170–84.
[19] Gordon J, Amini S, White MK. General overview of neuronal cell culture. Methods Mol Biol 2013;1078:1–8. http://dx.doi.org/10.1007/978-1-62703-640-5{_}1.
[20] Kunze A, Tseng P, Godzich C, Murray C, Caputo A, Schweizer FE, Carlo DD. Engineering cortical neuron polarity with nanomagnets on a chip. ACS Nano 2015;9:3664–76. http://dx.doi.org/10.1021/nn505330w.

[21] Bettencourt LM, Stephens GJ, Ham MI, Gross GW. Functional structure of cortical neuronal networks grown in vitro. Phys Rev E Stat Nonlinear Soft Matter Phys 2007;75(2):021915.

[22] Spira ME, Hai A. Multi-electrode array technologies for neuroscience and cardiology. Nature Nanotechnol 2013;8(2):83–94. http://dx.doi.org/10.1038/nnano.2012.265.

[23] de Santos-Sierra D, Sendiña-Nadal I, Leyva I, Almendral JA, Anava S, Ayali A, et al. Emergence of small-world anatomical networks in self-organizing clustered neuronal cultures. PLoS One 2014;9:e85828. http://dx.doi.org/10.1371/journal.pone.0085828.

[24] Schroeter MS, Charlesworth P, Kitzbichler MG, Paulsen O, Bullmore ET. Emergence of rich-club topology and coordinated dynamics in development of hippocampal functional networks in vitro. J Neurosci 2015;35(14):5459–70. http://dx.doi.org/10.1523/JNEUROSCI.4259-14.2015.

[25] Han Y, Zhu H, Zhao Y, Lang Y, Sun H, Han J, et al. The effect of acute glutamate treatment on the functional connectivity and network topology of cortical cultures. Med Eng Phys 2019;71:91–7. http://dx.doi.org/10.1016/J.MEDENGPHY.2019.07.007.

[26] Antonello PC, Varley TF, Beggs J, Porcionatto M, Sporns O, Faber J. Self-organization of in vitro neuronal assemblies drives to complex network topology. ELife 2022;11. http://dx.doi.org/10.7554/eLife.74921.

[27] Nieus T, D'Andrea V, Amin H, Di Marco S, Safaai H, Maccione A, et al. State-dependent representation of stimulus-evoked activity in high-density recordings of neural cultures. Sci Rep 2018;8(1):5578.

[28] Sun C, Lin KC, Yeung CY, Ching ESC, Huang Y-TT, Lai P-YY, et al. Revealing directed effective connectivity of cortical neuronal networks from measurements. Phys Rev E 2022;105(4):044406. http://dx.doi.org/10.1103/PhysRevE.105.044406.

[29] Soriano J, Martínez MR, Tlusty T, Moses E. Development of input connections in neural cultures. Proc Natl Acad Sci 2008;105:13758–63. http://dx.doi.org/10.1073/pnas.0707492105.

[30] Tibau E, Valencia M, Soriano J. Identification of neuronal network properties from the spectral analysis of calcium imaging signals in neuronal cultures. Front Neural Circuits 2013;7(DEC):199.

[31] Jia X, Shao W, Hu N, Shi J, Fan X, Chen C, et al. Learning populations with hubs govern the initiation and propagation of spontaneous bursts in neuronal networks after learning. Front Neurosci 2022;16(August):1–15. http://dx.doi.org/10.3389/fnins.2022.854199.

[32] Downes JH, Hammond MW, Xydas D, Spencer MC, Becerra VM, Warwick K, et al. Emergence of a small-world functional network in cultured neurons. PLoS Comput Biol 2012;8:e1002522. http://dx.doi.org/10.1371/journal.pcbi.1002522.

[33] Marconi E, Nieus T, Maccione A, Valente P, Simi A, Messa M, et al. Emergent functional properties of neuronal networks with controlled topology. PLoS One 2012;7:e34648. http://dx.doi.org/10.1371/journal.pone.0034648.

[34] Schröter M, Paulsen O, Bullmore ET. Micro-connectomics: probing the organization of neuronal networks at the cellular scale. Nat Rev Neurosci 2017;18(3):131–46.

[35] Eckmann JP, Feinerman O, Gruendlinger L, Moses E, Soriano J, Tlusty T. The physics of living neural networks. Phys Rep 2007;449:54–76. http://dx.doi.org/10.1016/J.PHYSREP.2007.02.014.

[36] Shein-Idelson M, Ben-Jacob E, Hanein Y. Engineered neuronal circuits: A new platform for studying the role of modular topology. Front Neuroeng 2011;4(SEPTEMBER):1–8. http://dx.doi.org/10.3389/fneng.2011.00010.

[37] Yamamoto H, Moriya S, Ide K, Hayakawa T, Akima H, Sato S, et al. Impact of modular organization on dynamical richness in cortical networks. Sci Adv 2018;4(11). http://dx.doi.org/10.1126/SCIADV.AAU4914/SUPPL{_}FILE/AAU4914{_}SM.PDF.

[38] Ludl A-A, Soriano J. Impact of physical obstacles on the structural and effective connectivity of in silico neuronal circuits. Front Comput Neurosci 2020;14:77.

[39] Anava S, Greenbaum A, Jacob EB, Hanein Y, Ayali A. The regulative role of neurite mechanical tension in network development. Biophys J 2009;96(4):1661–70. http://dx.doi.org/10.1016/j.bpj.2008.10.058.

[40] Anava S, Saad Y, Ayali A. The role of gap junction proteins in the development of neural network functional topology. Insect Mol Biol 2013;22:457–72. http://dx.doi.org/10.1111/imb.12036.

[41] Ayali A. Editorial: models of invertebrate neurons in culture. J Mol Histol 2012;43(4):379–81.

[42] Couzin-Fuchs E, Ayali A. The social brain of 'non-eusocial' insects. Curr Opin Insect Sci 2021;48:1–7. http://dx.doi.org/10.1016/j.cois.2021.04.006, NeuroScience . Special Section on Insects as food and feed.

[43] Shefi O, Golding I, Segev R, Ben-Jacob E, Ayali A. Morphological characterization of in vitro neuronal networks. Phys Rev E 2002;66:021905. http://dx.doi.org/10.1103/PhysRevE.66.021905.

[44] Greenbaum A, Anava S, Ayali A, Shein M, David-Pur M, Ben-Jacob E, et al. One-to-one neuron–electrode interfacing. J Neurosci Methods 2009;182(2):219–24. http://dx.doi.org/10.1016/j.jneumeth.2009.06.012.

[45] de Santos-Sierra D, Sendiña-Nadal I, Leyva I, Almendral JA, Ayali A, Anava S, et al. Graph-based unsupervised segmentation algorithm for cultured neuronal networks' structure characterization and modeling. Cytometry A 2015;87:513–23. http://dx.doi.org/10.1002/cyto.a.22591.

[46] de Santos-Sierra D, Leyva I, Almendral JA, Boccaletti S, Sendiña-Nadal I. Self-organized cultured neuronal networks: Longitudinal analysis and modeling of the underlying network structure. In: Carballido-Landeira J, Escribano B, editors. Biological systems: Nonlinear dynamics approach. Cham: Springer International Publishing; 2019, p. 59–85. http://dx.doi.org/10.1007/978-3-030-16585-7{_}4.

[47] Tlaie A, Ballesteros-Esteban L, Leyva I, Sendiña-Nadal I. Statistical complexity and connectivity relationship in cultured neural networks. Chaos Solitons Fractals 2019;119:284–90. http://dx.doi.org/10.1016/j.chaos.2018.12.027.

[48] Wagenaar DA, Pine J, Potter SM. An extremely rich repertoire of bursting patterns during the development of cortical cultures. BMC Neurosci 2006;7:11. http://dx.doi.org/10.1186/1471-2202-7-11.

[49] Fuchs E, Ayali A, Robinson A, Hulata E, Ben-Jacob E. Coemergence of regularity and complexity during neural network development. Dev Neurobiol 2007;67:1802–14. http://dx.doi.org/10.1002/dneu.20557.

[50] Burrows M. The neurobiology of an insect brain. Oxford University Press; 1996, http://dx.doi.org/10.1093/acprof:oso/9780198523444.001.0001.

[51] Herreros P, Ballesteros-Esteban LM, Laguna MF, Leyva I, Sendiña-Nadal I, Holgado M. Neuronal circuits on a chip for biological network monitoring. Biotechnol J 2021;16:2000355. http://dx.doi.org/10.1002/biot.202000355.

[52] Bocaletti S, Latora V, Moreno Y, M. C, Hwang D. Complex networks: Structure and dynamics. Phys Rep 2006;424:175–308. http://dx.doi.org/10.1016/j.physrep.2005.10.009.

[53] Rubinov M, Sporns O. Complex network measures of brain connectivity: uses and interpretations. Neuroimage 2010;52(3):1059–69.

[54] Rad AA, Sendiña-Nadal I, Papo D, Zanin M, Buldú JM, del Pozo F, et al. Topological measure locating the effective crossover between segregation and integration in a modular network. Phys Rev Lett 2012;108:228701. http://dx.doi.org/10.1103/PhysRevLett.108.228701.

[55] White JG, Southgate E, Thomson JN, Brenner S. The structure of the nervous system of the nematode *Caenorhabditis elegans*. Philos Trans R Soc Lond B Biol Sci 1986;314(1165):1–340. http://dx.doi.org/10.1098/rstb.1986.0056.

[56] Barthélemy M. Spatial networks. Phys Rep 2011;499(1–3):1–101. http://dx.doi.org/10.1016/j.physrep.2010.11.002, arXiv:1010.0302.

[57] Quian Quiroga R, Kreuz T, Grassberger P. Event synchronization: A simple and fast method to measure synchronicity and time delay patterns. Phys Rev E 2002;66:041904. http://dx.doi.org/10.1103/PhysRevE.66.041904.

[58] Leyva I, Navas A, Sendiña-Nadal I, Buldú JM, Almendral JA, Boccaletti S. Synchronization waves in geometric networks. Phys Rev E 2011;84:065101. http://dx.doi.org/10.1103/PhysRevE.84.065101.

[59] Pereda E, Quiroga RQ, Bhattacharya J. Nonlinear multivariate analysis of neurophysiological signals. Progr Neurobiol 2005;77(1):1–37. http://dx.doi.org/10.1016/j.pneurobio.2005.10.003.

[60] Korhonen O, Zanin M, Papo D. Principles and open questions in functional brain network reconstruction. Hum Brain Mapp 2021;42(11):3680–711. http://dx.doi.org/10.1002/hbm.25462.

[61] Silini R, Masoller C. Fast and effective pseudo transfer entropy for bivariate data-driven causal inference. Sci Rep 2021;11(1):8423. http://dx.doi.org/10.1038/s41598-021-87818-3.

[62] Ramakers GJ, van Galen H, Feenstra MG, Corner MA, Boer GJ. Activity-dependent plasticity of inhibitory and excitatory amino acid transmitter systems in cultured rat cerebral cortex. Int J Dev Neurosci 1994;12(7):611–21.

[63] van Pelt J, Vajda I, Wolters PS, Corner MA, Ramakers GJ. Dynamics and plasticity in developing neuronal networks in vitro. Progr Brain Res 2005;147:171–88. http://dx.doi.org/10.1016/S0079-6123(04)47013-7.

[64] Pernice V, Staude B, Cardanobile S, Rotter S. How structure determines correlations in neuronal networks. PLoS Comput Biol 2011;7(5):e1002059.

[65] Ton R, Deco G, Daffertshofer A. Structure-function discrepancy: Inhomogeneity and delays in synchronized neural networks. PLoS Comput Biol 2014;10:1–15. http://dx.doi.org/10.1371/journal.pcbi.1003736.

[66] Batista-García-Ramó K, Fernández-Verdecia CI. What we know about the brain structure–function relationship. Behav Sci 2018;8(4):39.

[67] Biswas T, Fitzgerald JE. Geometric framework to predict structure from function in neural networks. Phys Rev Res 2022;4:023255. http://dx.doi.org/10.1103/PhysRevResearch.4.023255.

[68] Cabrera-Garcia D, Warm D, de la Fuente P, Fernández-Sánchez MT, Novelli A, Villanueva-Balsera JM. Early prediction of developing spontaneous activity in cultured neuronal networks. Sci Rep 2021;11:20407. http://dx.doi.org/10.1038/s41598-021-99538-9.

[69] Papo D, Zanin M, Pineda-Pardo JA, Boccaletti S, Buldú JM. Functional brain networks: great expectations, hard times and the big leap forward. Philos Trans R Soc B 2014;369:20130525. http://dx.doi.org/10.1098/rstb.2013.0525.

[70] Ayali A, Zilberstein Y, Cohen N. The locust frontal ganglion: a central pattern generator network controlling foregut rhythmic motor patterns. J Exp Biol 2002;205:2825–32. http://dx.doi.org/10.1242/jeb.205.18.2825.

[71] Negri J, Menon V, Young-Pearse TL. Assessment of spontaneous neuronal activity in vitro using multi-well multi-electrode arrays: Implications for assay development. ENeuro 2020;7(1). http://dx.doi.org/10.1523/ENEURO.0080-19.2019, ENEURO.0080–19.2019.

[72] Stetter O, Battaglia D, Soriano J, Geisel T. Model-free reconstruction of excitatory neuronal connectivity from calcium imaging signals. PLoS Comput Biol 2012;8:e1002653. http://dx.doi.org/10.1371/journal.pcbi.1002653.